NONLINEAR BUCKLING BEHAVIOR OF FG-GPLRC CYLINDRICAL SHELL STIFFENED BY SPIRAL FG-GPLRC STIFFENERS SUBJECTED TO AXIAL COMPRESSIVE LOAD IN THERMAL ENVIRONMENT

Kieu Quang Thai[1], Dao Huy Bich[2], Nguyen Thi Phuong[3,4,*],
Cao Van Doan[5], Tran Quang Minh[5]

[1]*Graduate University of Science and Technology, Vietnam Academy of Science and Technology, Hanoi, Vietnam*
[2]*Faculty of Mathematics, Mechanics and Informatics, VNU University of Science, Hanoi, Vietnam*
[3]*Mechanics of Advanced Materials and Structures, Institute for Advanced Study in Technology,*
Ton Duc Thang University, Ho Chi Minh City, Vietnam
[4]*Faculty of Civil Engineering, Ton Duc Thang University, Ho Chi Minh City, Vietnam*
[5]*Mechanics of Advanced Materials and Structures, University of Transport Technology, Hanoi, Vietnam*
E-mail: nguyenthiphuong@tdtu.edu.vn

Abstract. This study investigates the nonlinear behavior of functionally graded graphene platelet-reinforced composite (FG-GPLRC) thin cylindrical shells stiffened by orthogonal or spiral FG-GPLRC stiffeners under axial compression. Five graphene platelet (GPL) distribution patterns for shell and stiffeners are considered. The governing equations are formulated based on Donnell shell theory, incorporating geometric nonlinearity of von Karman and the effects of Pasternak elastic foundation. The influence of spiral stiffeners is modeled using an improved Lekhnitskii smeared stiffener technique, considering both mechanical and thermal stresses. Circumferential closed conditions, three-term form of deflection, and the Ritz energy method are employed to derive expressions for the critical buckling load and postbuckling load-deflection curves. The results demonstrate that spiral stiffeners provide superior load-carrying capacity compared to orthogonal stiffeners. Numerical studies also show significant effects of thermal environment, material distribution patterns, geometric parameters, and elastic foundation on the buckling and postbuckling responses of stiffened shells.

Keywords: functionally graded graphene platelet-reinforced composite (FG-GPLRC), nonlinear buckling, spiral stiffener, Ritz energy method, cylindrical shell.

1. INTRODUCTION

Functionally graded materials (FGMs) have been widely applied in the aerospace, marine, and automotive industries due to their excellent thermomechanical properties, achieved through gradual changes in composition and microstructure. The nonlinear buckling and postbuckling behavior of functionally graded material (FGM) cylindrical shells has been extensively studied. Representative studies include H. Huang and Han (2009), Lu et al. (2025), Sofiyev and Kuruoglu (2014), and Shen (2005), who investigated complex stability responses under different types of loading using analytical frameworks such as Donnell shell theory with the Ritz method (H. Huang & Han, 2009), the Galerkin method (Lu et al., 2025; Sofiyev & Kuruoglu, 2014), and

higher-order shear deformation theory (HSDT) with singular perturbation techniques (Shen, 2005). Focusing on stiffened structures, Huy Bich et al. (2013) examined static and dynamic buckling of FGM cylindrical shells stiffened by orthogonal stiffeners under axial compressive load, Singh et al. (2025) analyzed the free vibration of cracked isotropic and FGM shells with axially varying thickness based on Donnell–Mushtari–Vlasov theory and the line spring model, considering the effect of localized defects on dynamic behavior. Nam et al. (2018) developed an analytical approach for the nonlinear stability problem of multilayer FGM shells with spiral FGM stiffeners by improving the smeared stiffener technique.

The stability of functionally graded carbon nanotube-reinforced composite (FG-CNTRC) cylindrical shells has been extensively investigated using different theoretical and numerical methodologies. The postbuckling behavior of axially and radially loaded FG-CNTRC cylindrical shells in thermal environments was analyzed by Shen (2011) and Shen and Xiang (2013), based on HSDT and singular perturbation techniques. A novel instability mode, referred to as snap-backward, was proposed (Nguyen et al., 2020) using isogeometric analysis. The basis formulations were established applying the first-order shear deformation theory (FSDT) and non-uniform rational B-Spline (NURBS) basis functions, the initial geometric imperfection and the von Kármán assumption were also taken into account. Lei et al. (2013) presented a large deflection analysis of FG-CNTRC plates using the element-free kp-Ritz method with effective material properties estimated using an equivalent continuum model based on the Eshelby–Mori–Tanaka approach. Dynamic buckling of FG-CNTRC shells under time-varying axial displacement was investigated by Jiao et al. (2019) applying a semi-analytical approach that combined the Galerkin and Runge-Kutta methods. The Budiansky-Roth criterion was applied to determine the dynamic critical buckling. Based on classical Donnell theory and the Galerkin method, Dong et al. (2022) examined the nonlinear buckling and postbuckling responses of stiffened FG-CNTRC cylindrical shells with CNT-stiffeners. The notable effects of stiffener configuration, CNT volume fraction, and foundation stiffness were reported.

Functionally graded graphene platelet-reinforced composites (FG-GPLRCs) have attracted attention due to their remarkable mechanical stiffness and superior thermal conductivity. Recently, many studies on the mechanical behavior of FG-GPLRC cylindrical shells have been published. The torsional and eigenvalue buckling responses of FG-GPLRC shells with cutouts and multilayered thickness configurations were examined by Wang, Feng, Zhao, Lu, and Yang (2018) and Wang, Feng, Zhao, and Yang (2018) using the finite element method, where the effective material properties were determined by the Halpin-Tsai approach. The obtained results showed significant effects of graphene platelet (GPL) distribution patterns and geometrical imperfections on the buckling load and mode transitions. A semi-analytical variational framework was developed by Ansari and Torabi (2019) using FSDT and the variational differential quadrature method to obtain nonlinear postbuckling behavior and secondary bifurcations with different GPL distribution patterns and weight fractions. A three-dimensional elasticity-based state-space formulation was employed by Liu et al. (2018) to analyze the buckling and vibration of initially stressed FG-GPLRC shells, and analytical solutions were derived for different GPL distribution patterns. Thermo-elastic responses of circumferentially closed FG-GPLRC cylindrical shells were analyzed by X. Huang et al. (2021), in which analytical models incorporating thermal boundary conditions and displacement continuity were constructed. Ramezani et al. (2022) presented a nonlinear thermomechanical analysis using HSDT enriched with quasi-3D ANS cover functions, where temperature-dependent properties and geometric nonlinearity were taken into account in the governing equations, and the analytical model was validated based on single-layer theories. The influences of geometric, thermal, and material parameters on postbuckling behavior were investigated.

This paper presents a novel investigation into the nonlinear buckling behavior of FG-GPLRC thin cylindrical shells stiffened by orthogonal and spiral FG-GPLRC stiffeners. An

improved smeared stiffener model is applied to spiral stiffeners, fully incorporating thermal and mechanical effects. The study also employs a circumferentially closed condition combined with the Ritz method to derive critical load and postbuckling relationships. The results show the superior performance of spiral stiffeners and the strong influence of material distribution pattern and temperature on the load-carrying capacity of the structure.

2. THE COORDINATE SYSTEM, SPIRAL STIFFENERS, AND GPL DISTRIBUTION PATTERNS

Consider a FG-GPLRC thin cylindrical shell subjected to uniform axial compressive load P and resting on a two-parameter elastic foundation in a thermal environment. The geometric configuration of the cylindrical shell includes the mean radius a, thickness h, and length L, defined in a cylindrical coordinate system illustrated in Fig. 1. The x- and y-axes correspond to the longitudinal and circumferential directions, respectively, while the z-axis represents the thickness axis. The coordinate η is introduced to describe the local orientation along the spiral stiffeners. The shell–foundation interaction is described by the Pasternak foundation model, including Winkler stiffness K_1 and shear stiffness K_2.

The material behavior is governed by an effective modulus approach for FG-GPLRCs, incorporating the Halpin-Tsai model to estimate the equivalent elastic properties, determined as

$$E_{(z)} = \frac{3}{8} E_m \frac{1 + \xi_L V_{GPL(z)} \eta_L}{1 - \eta_L V_{GPL(z)}} + \frac{5}{8} E_m \frac{1 + \xi_W V_{GPL(z)} \eta_W}{1 - \eta_W V_{GPL(z)}}, \tag{1}$$

where

$$\eta_W = \frac{(E_{GPL}/E_m) - 1}{(E_{GPL}/E_m) + \xi_W}, \quad \eta_L = \frac{(E_{GPL}/E_m) - 1}{(E_{GPL}/E_m) + \xi_L}, \quad \xi_W = \frac{2w_{GPL}}{t_{GPL}}, \quad \xi_L = \frac{2L_{GPL}}{t_{GPL}}, \tag{2}$$

and E_m and E_{GPL} indicate the elastic modulus of the matrix and GPLs. L_{GPL} is GPL length, and GPL thickness and width are denoted by t_{GPL} and w_{GPL}, respectively. V_{GPL} is the volume fraction of the GPLs ($V_{GPL} + V_m = 1$), derived by

$$V_{GPL}(z) = \frac{W_{GPL}}{W_{GPL} + (1 - W_{GPL})(\rho_{GPL}/\rho_M)}, \tag{3}$$

in which the mass densities of the GPLs and the matrix are denoted by ρ_{GPL} and ρ_M, respectively.
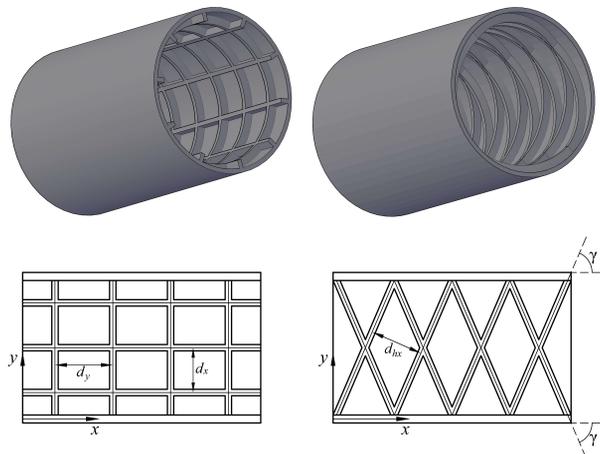

Fig. 1. Configurations of cylindrical shells stiffened by orthogonal and spiral stiffeners

Five GPL distribution patterns of the mass fraction of GPLs W_{GPL} for the shell and stiffener, respectively, are designed as

- UD distribution pattern (UD shell with UD stiffener)

$$W_{GPL} = W_{GPL}^*, \quad W_{GPL} = W_{GPL}^*, \tag{4}$$

- FG-X distribution pattern (FG-X shell with FG-X stiffener)

$$W_{GPL} = \frac{4\,|z|\,W_{GPL}^*}{h}, \quad W_{GPL} = \left[\left(\frac{2h - 4z}{h_{St}} + 2\right)\right] W_{GPL}^*, \tag{5}$$

- FG-O distribution pattern (FG-O shell with FG-O stiffener)

$$W_{GPL} = \left(2 - \frac{4\,|z|}{h}\right) W_{GPL}^*, \quad W_{GPL} = \left[2 - \left|\left(\frac{4z - 2h}{h_{St}} - 2\right)\right|\right] W_{GPL}^*, \tag{6}$$

- FG-V distribution pattern (FG-V shell with FG-A stiffener)

$$W_{GPL} = \left(1 - \frac{2z}{h}\right) W_{GPL}^*, \quad W_{GPL} = \left[\frac{2z - h}{h_{St}}\right] W_{GPL}^*, \tag{7}$$

- FG-A distribution pattern (FG-A shell with FG-V stiffener)

$$W_{GPL} = \left(1 + \frac{2z}{h}\right) W_{GPL}^*, \quad W_{GPL} = \left[2 + \frac{(h - 2z)}{h_{St}}\right] W_{GPL}^*, \tag{8}$$

According to the mixture rule, the effective Poisson's ratio and thermal expansion coefficient of the FG-GPLRC are expressed as follows

$$\nu_{(z)} = \nu_m \left(1 - V_{GPL}\right) + \nu_{GPL} V_{GPL}, \quad \alpha_{(z)} = \alpha_m \left(1 - V_{GPL}\right) + \alpha_{GPL} V_{GPL}, \tag{9}$$
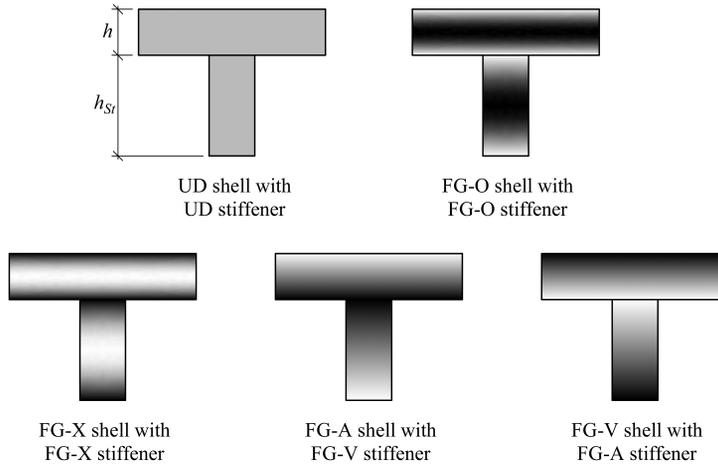

Fig. 2. Distribution patterns of GPL in shells and stiffeners

3. GOVERNING FORMULATIONS

According to the Donnell shell theory with the geometrical nonlinearities of von Karman theory, the strain components at a distance z from the middle surface can be written as

$$\left\{\begin{array}{c} \varepsilon_x \\ \varepsilon_y \\ \gamma_{xy} \end{array}\right\} = \left\{\begin{array}{c} \varepsilon_{0x} \\ \varepsilon_{0y} \\ \gamma_{0xy} \end{array}\right\} - z \left\{\begin{array}{c} w_{,xx} \\ w_{,yy} \\ 2w_{,xy} \end{array}\right\}, \tag{10}$$

where ε_x, ε_y, and γ_{xy} are the normal and shear strain components.

The relation between mid-plane strains ε_{0x}, ε_{0y}, γ_{0xy} and displacements u, v, and w can be applied in nonlinear forms, as

$$\varepsilon_{0x} = u_{,x} + \frac{w_{,x}^2}{2}, \quad \varepsilon_{0y} = v_{,y} + \frac{w_{,y}^2}{2} - \frac{w}{a}, \quad \gamma_{0xy} = u_{,y} + w_{,x}w_{,y} + v_{,x}, \tag{11}$$

The deformation compatibility equation can be obtained from Eq. (11), as

$$\varepsilon_{0y,xx} + \varepsilon_{0x,yy} - \gamma_{0xy,xy} = -\frac{w_{,xx}}{a} + \left(w_{,xy}\right)^2 - w_{,yy}w_{,xx}. \tag{12}$$

Hooke's law of orthotropic structures can be applied to the FG-GPLRC cylindrical shell and is written as

$$\begin{bmatrix} \sigma_{xx} \\ \sigma_{yy} \\ \sigma_{xy} \end{bmatrix} = \begin{bmatrix} Q_{11SH} & Q_{12SH} & 0 \\ Q_{12SH} & Q_{22SH} & 0 \\ 0 & 0 & Q_{66SH} \end{bmatrix} \begin{bmatrix} \varepsilon_x - \Delta T \alpha_{11} \\ \varepsilon_y - \Delta T \alpha_{22} \\ \gamma_{xy} \end{bmatrix}, \tag{13}$$

with

$$Q_{11SH} = \frac{E_{(z)}}{1 - \nu_{(z)}^2}, \quad Q_{12SH} = \frac{E_{(z)}\nu_{(z)}}{1 - \nu_{(z)}^2}, \quad Q_{22SH} = \frac{E_{(z)}}{1 - \nu_{(z)}^2}, \quad Q_{66SH} = G_{12}, \tag{14}$$

where Q_{ij} are defined to be reduced stiffnesses, and the temperature change ΔT is assumed to be uniformly distributed.

By combining the coordinate transformation technique and anisotropic beam theory, the spiral FG-GLPRC stiffeners are modeled through the additional stiffnesses taking into account the thermal stresses in shells and stiffeners. By integrating Hooke's law (13), the forces and moments of the shell can be obtained, taking into account the improved smeared spiral stiffener technique, presented by

$$\begin{Bmatrix} N_x \\ N_y \\ N_{xy} \\ M_x \\ M_y \\ M_{xy} \end{Bmatrix} = \begin{Bmatrix} A_{11} & A_{12} & 0 & B_{11} & B_{12} & 0 \\ A_{21} & A_{22} & 0 & B_{21} & B_{22} & 0 \\ 0 & 0 & A_{66} & 0 & 0 & B_{66} \\ B_{11} & B_{12} & 0 & D_{11} & D_{12} & 0 \\ B_{21} & B_{22} & 0 & D_{21} & D_{22} & 0 \\ 0 & 0 & B_{66} & 0 & 0 & D_{66} \end{Bmatrix} \begin{Bmatrix} \varepsilon_{0x} \\ \varepsilon_{0y} \\ \gamma_{0xy} \\ -w_{,xx} \\ -w_{,yy} \\ -2w_{,xy} \end{Bmatrix} + \begin{Bmatrix} \Phi_{1x} \\ \Phi_{1y} \\ 0 \\ \Phi_{2x} \\ \Phi_{2y} \\ 0 \end{Bmatrix}, \tag{15}$$

where $\left(A_{ij}, B_{ij}, D_{ij}\right)$ are defined to be the stiffnesses of the cylindrical shells with spiral stiffeners, expressed by

$$A_{22} = A_{22SH} + \mu_2 \frac{b_y}{d_y} A_{11}^{ST} + 2\mu_3 \sin^4 \gamma \frac{b_{hx}}{d_{hx}} A_{11}^{ST}, \quad A_{66} = A_{66SH} + 2\mu_3 \cos^2 \gamma \sin^2 \gamma \frac{b_{hx}}{d_{hx}} A_{11}^{ST},$$

$$A_{11} = A_{11SH} + \mu_1 \frac{b_x}{d_x} A_{11}^{ST} + 2\mu_3 \cos^4 \gamma \frac{b_{hx}}{d_{hx}} A_{11}^{ST}, \quad A_{12} = A_{12SH} + 2\mu_3 \cos^2 \gamma \sin^2 \gamma \frac{b_{hx}}{d_{hx}} A_{11}^{ST}, \tag{16}$$

$$B_{22} = B_{22SH} + \mu_2 \frac{b_y}{d_y} B_{11}^{ST} + 2\mu_3 \frac{b_{hx}}{d_{hx}} B_{11}^{ST} \sin^4 \gamma, \quad B_{66} = B_{66SH} + 2\mu_3 \frac{b_{hx}}{d_{hx}} B_{11}^{ST} \cos^2 \gamma \sin^2 \gamma,$$

$$B_{11} = B_{11SH} + \mu_1 \frac{b_x}{d_x} B_{11}^{ST} + 2\mu_3 \frac{b_{hx}}{d_{hx}} B_{11}^{ST} \cos^4 \gamma, \quad B_{12} = B_{12SH} + 2\mu_3 \frac{b_{hx}}{d_{hx}} B_{11}^{ST} \cos^2 \gamma \sin^2 \gamma, \tag{17}$$

$$D_{22} = D_{22SH} + \mu_2 \frac{b_y}{d_y} D_{11}^{ST} + 2\mu_3 \sin^4 \gamma \frac{b_{hx}}{d_{hx}} D_{11}^{ST}, \quad D_{66} = D_{66SH} + 2\mu_3 \cos^2 \gamma \sin^2 \gamma \frac{b_{hx}}{d_{hx}} D_{11}^{St},$$

$$D_{11} = D_{11SH} + \mu_1 \frac{b_x}{d_x} D_{11}^{ST} + 2\mu_3 \frac{b_{hx}}{d_{hx}} \cos^4 \gamma D_{11}^{ST}, \quad D_{12} = D_{12SH} + 2\mu_3 \cos^2 \gamma \sin^2 \gamma \frac{b_{hx}}{d_{hx}} D_{11}^{ST}, \tag{18}$$

with b_x, b_y, b_{hx} and d_x, d_y, d_{hx} are the widths and distances between neighbouring stiffeners of longitudinal, circumferential, and spiral stiffeners, $\gamma = \arccos\left(n_{hx}d_{hx}/2\pi a\right)$ is the spiral stiffener angle (Nam et al., 2018), with the number of spiral stiffeners n_{hx} and

$$\left(A_{ijSH}, B_{ijSH}, D_{ijSH} \right) = \int_{\Pi} Q_{ij} \left(1, z, z^2 \right) dz, \quad (i, j = 1, 2, 6),$$

$$\begin{bmatrix} A_{11}^{ST} & B_{11}^{ST} \\ B_{11}^{ST} & D_{11}^{ST} \end{bmatrix} = \begin{bmatrix} \bar{A}_{11} & \bar{B}_{11} \\ \bar{B}_{11} & \bar{D}_{11} \end{bmatrix} - \begin{bmatrix} \bar{A}_{12} & 0 & \bar{B}_{12} & 0 \\ \bar{B}_{12} & 0 & \bar{D}_{12} & 0 \end{bmatrix} \begin{bmatrix} \bar{A}_{22} & 0 & \bar{B}_{22} & 0 \\ 0 & \bar{A}_{66} & 0 & \bar{B}_{66} \\ \bar{B}_{22} & 0 & \bar{D}_{22} & 0 \\ 0 & \bar{B}_{66} & 0 & \bar{D}_{66} \end{bmatrix}^{-1} \begin{bmatrix} \bar{A}_{12} & \bar{B}_{12} \\ 0 & 0 \\ \bar{B}_{12} & \bar{D}_{12} \\ 0 & 0 \end{bmatrix}, \quad (19)$$

where Π is the thickness domain of the FG-GPLRC cylindrical shell, and

$$\left(\bar{A}_{ij}, \bar{B}_{ij}, \bar{D}_{ij} \right) = \int_{\Delta} Q_{ij} \left(1, z, z^2 \right) dz, \quad (i, j = 1, 2, 6), \tag{20}$$

with Δ is the height domain of the stiffeners.

The thermal forces of the stiffened shells are expressed by

$$\Phi_{1x} = \Phi_{1x}^{SH} + \gamma_1 \frac{b_x}{d_x} \Phi_{1x}^{ST} + 2\gamma_3 \frac{b_{hx}}{d_{hx}} \Phi_{1x}^{ST} \left(\cos^2 \gamma \sin^4 \gamma + \cos^4 \gamma \sin^2 \gamma + \cos^6 \gamma \right),$$

$$\Phi_{1y} = \Phi_{1y}^{SH} + \gamma_2 \frac{b_y}{d_y} \Phi_{1x}^{ST} + 2\gamma_3 \frac{b_{hx}}{d_{hx}} \Phi_{1x}^{ST} \left(\sin^2 \gamma \cos^4 \gamma + \sin^4 \gamma \cos^2 \gamma + \sin^6 \gamma \right), \tag{21}$$

where

$$\Phi_{1y}^{SH} = \Delta T \int_{\Pi} (Q_{22}\alpha_{22} + Q_{12}\alpha_{11})dz, \quad \Phi_{1x}^{SH} = \Delta T \int_{\Pi} (Q_{12}\alpha_{22} + Q_{11}\alpha_{11})dz,$$

$$\Phi_{1x}^{ST} = \Delta T \int_{\Delta} (Q_{12}\alpha_{22} + Q_{11}\alpha_{11})dz, \tag{22}$$

From Eq. (15), the inverse relations can be obtained by

$$\varepsilon_{0x} = A_{12}^* \left(N_y - \Phi_{1y} \right) + B_{12}^* w_{,yy} + B_{11}^* w_{,xx} + A_{11}^* \left(N_x - \Phi_{1x} \right),$$

$$\gamma_{0xy} = 2w_{,xy} B_{66}^* + N_{xy} A_{66}^*,$$

$$\varepsilon_{0y} = A_{22}^* \left(N_y - \Phi_{1y} \right) + B_{22}^* w_{,yy} + B_{21}^* w_{,xx} + A_{21}^* \left(N_x - \Phi_{1x} \right), \tag{23}$$

$$M_x = X_{12} \left(N_y - \Phi_{1y} \right) + S_{12} w_{,yy} + \Phi_{2x} + X_{11} \left(N_x - \Phi_{1x} \right) + S_{11} w_{,xx},$$

$$M_{xy} = 2S_{66} w_{,xy} + N_{xy} X_{66},$$

$$M_y = X_{22} \left(N_y - \Phi_{1y} \right) + S_{22} w_{,yy} + \Phi_{2y} + \left(N_x - \Phi_{1x} \right) X_{21} + S_{21} w_{,xx}, \tag{24}$$

where

$$A_{21}^* = -\frac{A_{21}}{\kappa_1}, \quad A_{22}^* = \frac{A_{11}}{\kappa_1}, \quad B_{22}^* = \frac{B_{22}A_{11} - A_{21}B_{12}}{\kappa_1}, \quad B_{21}^* = \frac{B_{21}A_{11} - A_{21}B_{11}}{\kappa_1},$$

$$B_{66}^* = \frac{B_{66}}{A_{66}}, \quad A_{66}^* = A_{66}^{-1}, \quad A_{12}^* = -\frac{A_{12}}{\kappa_1}, \quad A_{11}^* = \frac{A_{22}}{\kappa_1}, \quad B_{11}^* = \frac{B_{11}A_{22} - A_{12}B_{21}}{\kappa_1},$$

$$B_{12}^* = \frac{A_{22}B_{12} - B_{22}A_{12}}{\kappa_1}, \quad \kappa_1 = A_{11}A_{22} - A_{12}A_{21}, \quad X_{12} = A_{12}^* B_{11} + B_{12}A_{22}^*,$$

$$X_{11} = B_{11}A_{11}^* + A_{21}^* B_{12}, \quad X_{22} = B_{21}A_{12}^* + A_{22}^* B_{22}, \quad S_{12} = B_{11}B_{12}^* - D_{12} + B_{22}^* B_{12},$$

$$S_{11} = B_{11}B_{11}^* - D_{11} + B_{21}^* B_{12}, \quad S_{22} = B_{21}B_{12}^* - D_{22} + B_{22}^* B_{22}, \quad X_{21} = B_{21}A_{11}^* + B_{22}A_{21}^*,$$

$$S_{66} = B_{66}B_{66}^* - D_{66}, \quad S_{21} = B_{21}B_{11}^* - D_{21} + B_{21}^* B_{22}, \quad X_{66} = B_{66}A_{66}^*.$$

Introducing the stress function $\mu(x, y)$, which satisfies three conditions, as

$$N_x = \mu_{,yy}, N_{xy} = -\mu_{,xy}, N_y = \mu_{,xx}. \tag{25}$$

Substituting Eq. (25) into Eq. (12), another form of the deformation compatibility equation can be expressed by

$$
\begin{aligned}
\varphi \equiv {} & A_{22}^* \mu_{,xxxx} + \left(A_{12}^* + A_{66}^* + A_{21}^*\right) \mu_{,xxyy} + A_{11}^* \mu_{,yyyy} + B_{21}^* w_{,xxxx} + B_{12}^* w_{,yyyy} \\
& + w_{,xx} \left(w_{,yy} + \frac{1}{a}\right) + \left(B_{11}^* - 2B_{66}^* + B_{22}^*\right) w_{,xxyy} - \left(w_{,xy}\right)^2 = 0.
\end{aligned}
\tag{26}
$$

The simply supported boundary conditions are considered for cylindrical shells. The deflection of shells can be expressed in the three-term form, as (H. Huang & Han, 2009)

$$
w = f_0 + f_1 \sin\left(\frac{m\pi x}{L}\right) \sin\left(\frac{ny}{a}\right) + f_2 \left(\sin\left(\frac{m\pi x}{L}\right)\right)^2,
\tag{27}
$$

where m and n are the buckling modes in the longitudinal and circumferential directions, respectively. The prebuckling, linear, and nonlinear postbuckling deflection amplitudes are defined to be f_0, f_1, and f_2, respectively.

Substituting Eq. (27) into Eq. (26) and applying the harmonic balance method, the stress function is determined as

$$
\begin{aligned}
\varphi = {} & \varphi_1 \cos\left(\frac{2m\pi x}{L}\right) + \varphi_2 \cos\left(\frac{2ny}{a}\right) + \varphi_3 \sin\left(\frac{m\pi x}{L}\right) \sin\left(\frac{ny}{a}\right) \\
& + \varphi_4 \sin\left(\frac{3m\pi x}{L}\right) \sin\left(\frac{ny}{a}\right) - \frac{\sigma_{0y}}{2} hx^2 - \frac{P}{2} hy^2,
\end{aligned}
\tag{28}
$$

where the average circumferential stress of the cylindrical shells is defined to be σ_{oy}, and

$$
\varphi_1 = c_1 f_1^2 + c_2 f_2, \quad \varphi_2 = c_3 f_1^2, \quad \varphi_3 = c_4 f_1 f_2 + c_5 f_1, \quad \varphi_4 = c_6 f_1 f_2,
$$

$$
c_1 = \frac{L^2 n^2}{A_{22}^* \pi^2 m^2 a^2}, \quad c_2 = \frac{1}{8} \frac{4\pi^2 a m^2 B_{21}^* - L^2}{a A_{22}^* \pi^2 m^2}, \quad c_3 = \frac{1}{32} \frac{\pi^2 a^2 m^2}{L^2 n^2 A_{11}^*},
$$

$$
c_4 = -\frac{L^2 \pi^2 a^2 m^2 n^2}{\pi^4 a^4 m^4 A_{22}^* + L^2 a^2 m^2 n^2 \left(A_{66}^* + A_{12}^* + A_{21}^*\right) \pi^2 + L^4 n^4 A_{11}^*},
$$

$$
c_5 = \frac{-n^4 B_{12}^* L^4 - m^2 \left(-a + n^2 \left(B_{11}^* + B_{22}^* - 2B_{66}^*\right)\right) \pi^2 a^2 L^2 - \pi^4 a^4 m^4 B_{21}^*}{\pi^4 a^4 m^4 A_{22}^* + L^2 a^2 m^2 n^2 \left(A_{66}^* + A_{12}^* + A_{21}^*\right) \pi^2 + L^4 n^4 A_{11}^*},
$$

$$
c_6 = \frac{L^2 \pi^2 a^2 m^2 n^2}{81\pi^4 a^4 m^4 A_{22}^* + 9L^2 a^2 m^2 n^2 \left(A_{66}^* + A_{12}^* + A_{21}^*\right) \pi^2 + L^4 n^4 A_{11}^*},
$$

Due to the circumferential closed property of cylindrical shells, the following conditions are added, as (H. Huang & Han, 2009)

$$
\int_0^{2\pi a} \int_0^L \frac{\partial v}{\partial y} dx dy = \int_0^{2\pi a} \int_0^L \left(\varepsilon_{0y} + \frac{w}{a} - 0.5 w_{,y}^2\right) dx dy = 0.
\tag{29}
$$

After some calculations, the expression σ_{0y} can be found in (29) as

$$
\sigma_{0y} = b_3 f_1^2 + b_1 P + b_2 f_0 + b_4 f_2 + b_0,
\tag{30}
$$

where

$$
b_0 = \frac{-\Phi_{1x} A_{21}^* - \Phi_{1y} A_{22}^*}{A_{22}^* h}, \quad b_1 = -\frac{A_{21}^*}{A_{22}^*}, \quad b_2 = \frac{1}{h A_{22}^* a}, \quad b_3 = -\frac{n^2}{8 A_{22}^* h a^2}, \quad b_4 = \frac{1}{2} \frac{1}{h A_{22}^* a}.
$$

The strain energy is expressed by

$$
U_{in} = \frac{1}{2} \int_{-\frac{h}{2}}^{\frac{h}{2}} \int_0^{2\pi a} \int_0^L \left(\sigma_x \left(\varepsilon_x - \alpha_T \Delta T\right) + \sigma_y \left(\varepsilon_y - \alpha_T \Delta T\right) + \sigma_{xy} \left(\gamma_{xy} - \alpha_T \Delta T\right)\right) dx dy dz,
\tag{31}
$$

Substituting Eqs. (10), (13), and (30) into Eq. (31), then mathematical transformations are performed, leading to the new form of strain energy, as

$$
\begin{aligned}
U_{in} = {} & e_1 f_1^4 + e_2 f_1^2 f_2^2 + d_3 P f_1^2 + d_7 f_0 f_1^2 + e_4 f_2 f_1^2 + d_1 P^2 + d_2 P f_0 + d_4 P f_2 + d_6 f_0^2 \\
& + d_8 f_0 f_2 + e_3 f_2^2 + e_6 f_1^2 + d_5 P + d_9 f_0 + e_5 f_2 + e_7 + g_2 f_1^2 + g_1 f_0 + g_3 f_2 + g_0 P + g_4,
\end{aligned}
\tag{32}
$$

where

$$
d_1 = \pi \left(b_1^2 A_{22}^* + b_1 A_{12}^* + b_1 A_{21}^* + A_{11}^* \right) h^2 La, \quad d_2 = \pi \left(2 b_2 b_1 A_{22}^* + (A_{12}^* + A_{21}^*) b_2 \right) h^2 La,
$$

$$
d_3 = 2\pi h^2 b_3 \left(b_1 A_{22}^* + A_{12}^*/2 + A_{21}^*/2 \right) La, \quad d_4 = 2\pi h^2 b_4 \left(b_1 A_{22}^* + A A_{12}^*/2 + A_{21}^*/2 \right) La,
$$

$$
d_5 = \pi h \left((2 b_0 b_1 A_{22}^* + (A_{12}^* + A_{21}^*) b_0) h + \Phi_{1y} b_1 A_{22}^* + \Phi_{1x} b_1 A_{21}^* + \Phi_{1x} A_{11}^* + \Phi_{1y} A_{12}^* \right) La,
$$

$$
d_6 = \pi b_2^2 A_{22}^* h^2 La, \quad d_7 = 2\pi h^2 b_3 b_2 A_{22}^* La, \quad d_8 = 2\pi h^2 b_4 b_2 A_{22}^* La,
$$

$$
d_9 = \pi h \left(2 b_0 b_2 h A_{22}^* + \Phi_{1x} b_2 A_{21}^* + \Phi_{1y} b_2 A_{22}^* \right) La,
$$

$$
e_1 = \pi \left(\left(8\pi^4 c_1^2 m^4 A_{22}^* + L^4 b_3^2 h^2 A_{22}^* \right) a^4 + 8 L^4 c_3^2 A_{11}^* n^4 \right) \Big/ \left(L^3 a^3 \right),
$$

$$
e_2 = \frac{\pi}{4 L^3 a^3} \left(\begin{array}{l} A_{22}^* \left(81 c_6^2 + c_4^2 \right) m^4 \pi^4 a^4 + L^2 \pi^2 \left(9 c_6^2 + c_4^2 \right) m^2 \left(A_{12}^* + A_{21}^* + A_{66}^* \right) n^2 a^2 \\ + n^4 A_{11}^* \left(c_4^2 + c_6^2 \right) L^4 \end{array} \right),
$$

$$
e_3 = \frac{\pi \left(b_4^2 A_{22}^* h^2 L^4 + 8 m^4 \pi^4 \left(A_{22}^* c_2^2 + 0.5 c_2 X_{12} - 0.5 B_{21}^* c_2 - S_{11}/4 \right) \right) a}{L^3},
$$

$$
\begin{aligned}
e_4 = {} & 2\pi L a b_4 A_{22}^* h^2 b_3 + 16 \frac{\pi^5 a \left(A_{22}^* c_2 - B_{21}^*/4 + X_{12}/4 \right) m^4 c_1}{L^3} \\
& - \frac{1}{4} \frac{\pi L n^4 c_4 \left(-2 c_5 A_{11}^* + X_{21} - B_{12}^* \right)}{a^3} + \frac{1}{2} \frac{\left(A_{12}^* + A_{21}^* + A_{66}^* \right) c_4 n^2 \pi^3 m^2 c_5}{La} \\
& + \frac{1}{2} \frac{\left(X_{66} + B_{11}^*/2 + B_{22}^*/2 - B_{66}^* - X_{11}/2 - X_{22}/2 \right) c_4 n^2 \pi^3 m^2}{La} \\
& + \frac{1}{2} \frac{\pi^5 a c_4 \left(A_{22}^* c_5 + B_{21}^*/2 - X_{12}/2 \right) m^4}{L^3},
\end{aligned}
$$

$$
e_5 = \pi h \left(2 b_0 b_4 A_{22}^* h + b_4 \left(\Phi_{1x} A_{21}^* + \Phi_{1y} A_{22}^* \right) \right) La,
$$

$$
\begin{aligned}
e_6 = {} & 2\pi L a b_3 h^2 b_0 A_{22}^* + \pi L a b_3 h \Phi_{1x} A_{21}^* + \pi L a b_3 h \Phi_{1y} A_{22}^* - \frac{n^2 \left(S_{12} + S_{21} + 4 S_{66} \right) \pi^3 m^2}{4 La} \\
& - \frac{n^2 \left(-A_{12}^* - A_{21}^* - A_{66}^* \right) \pi^3 m^2 c_5^2}{4 La} - \frac{n^2 \left(X_{11} + X_{22} - 2 X_{66} - B_{11}^* - B_{22}^* + 2 B_{66}^* \right) \pi^3 m^2 c_5}{4 La} \\
& + \frac{\pi L n^4 \left(c_5^2 A_{11}^* + (-X_{21} + B_{12}^*) c_5 - S_{22} \right)}{4 a^3} + \frac{\pi^5 a m^4 \left(A_{22}^* c_5^2 + (-X_{12} + B_{21}^*) c_5 - S_{11} \right)}{4 L^3},
\end{aligned}
$$

$$
e_7 = \pi h \left(b_0^2 h A_{22}^* + \Phi_{1x} b_0 A_{21}^* + \Phi_{1y} b_0 A_{22}^* \right) La,
$$

$$
g_0 = \left(\left(b_1 A_{12}^* + A_{11}^* \right) \Phi_{1x}^* + \left(b_1 A_{22}^* + A_{21}^* \right) \Phi_{1y}^* \right) h \pi a L,
$$

$$
g_1 = \left(b_2 A_{12}^* \Phi_{1x}^* + b_2 A_{22}^* \Phi_{1y}^* \right) h \pi a L, g_2 = \left(b_3 A_{12}^* \Phi_{1x}^* + b_3 A_{22}^* \Phi_{1y}^* \right) h \pi a L,
$$

$$
g_3 = \left(b_4 A_{12}^* \Phi_{1x}^* + b_4 A_{22}^* \Phi_{1y}^* \right) h \pi a L,
$$

$$
g_4 = \left(\left(b_0 A_{12}^* \Phi_{1x}^* + b_0 A_{22}^* \Phi_{1y}^* \right) h + \left(\Phi_{1x} A_{11}^* + \Phi_{1y} A_{12}^* \right) \Phi_{1x}^* + \Phi_{1y}^* \left(\Phi_{1x} A_{21}^* + \Phi_{1y} A_{22}^* \right) \right) \pi a L.
$$

Taking into account Eqs. (11) and (23), the work done by the axial compressive load and foundation interaction is expressed by

$$U_{ext} = \int\limits_{0}^{2\pi a} \int\limits_{0}^{L} \left[-\frac{1}{2} w \left(K_1 w - K_2 \left(w_{,xx} + w_{,yy} \right) \right) \right] \mathrm{d}x \mathrm{d}y - Ph \int\limits_{0}^{2\pi a} \int\limits_{0}^{L} \left[\varepsilon_{0x} - \frac{1}{2} w_{,x}^2 \right] \mathrm{d}x \mathrm{d}y. \tag{33}$$

Substituting Eq. (27) into Eq. (33), the expression is rewritten by

$$U_{ext} = -\pi K_1 L a f_0^2 - \pi L a K_1 f_2 f_0 + g_7 P f_1^2 + g_5 P f_2^2 + g_8 P f_0 + h_2 f_1^2 + h_1 f_2^2 + g_6 P f_2 + g_9 P^2 + g_{10} P, \tag{34}$$

where

$$g_5 = \frac{\pi^3 m^2 h a}{2L}, \quad g_6 = 2\pi A_{12}^* b_4 h^2 L a, \quad g_7 = \frac{\pi h \left(8 A_{12}^* b_3 h L^2 + m^2 \pi^2 \right) a}{4L}, \quad g_8 = 2\pi L b_2 h^2 A_{12}^* a,$$

$$g_9 = 2\pi h^2 \left(b_1 A_{12}^* + A_{11}^* \right) L a, \quad g_{10} = 2\pi h \left(b_0 h A_{12}^* + \Phi_{1x} A_{11}^* + \Phi_{1y} A_{12}^* \right) L a,$$

$$h_1 = -\frac{3}{8} \frac{\left(4/3 m^2 \pi^2 K_2 + K_1 L^2 \right) \pi a}{L}, \quad h_2 = -\frac{\left(K_2 \pi^2 a^2 m^2 + a^2 K_1 L^2 + K_2 L^2 n^2 \right) \pi}{4La},$$

The total potential energy of shells is expressed by

$$U_{total} = U_{in} - U_{ext}. \tag{35}$$

By minimizing the total potential energy, a system of nonlinear algebraic equations is derived and solved iteratively to obtain the critical buckling loads and postbuckling curves. Substituting Eqs. (32) and (34) into Eq. (35) and applying the Ritz energy method leads to

$$\frac{\partial U_{total}}{\partial f_0} = 0, \quad \frac{\partial U_{total}}{\partial f_1} = 0, \quad \frac{\partial U_{total}}{\partial f_2} = 0, \tag{36}$$

leads to

$$2K_1 L \pi a f_0 + K_1 L \pi a f_2 + d_7 f_1^2 + d_2 P + 2d_6 f_0 + d_8 f_2 - g_8 P + d_9 + g_1 = 0, \tag{37}$$

$$2e_1 f_1^2 + e_2 f_2^2 + e_4 f_2 + (d_3 - g_7) P + d_7 f_0 + g_2 - h_2 + e_6 = 0, \tag{38}$$

$$K_1 L \pi a f_0 + 2e_2 f_1^2 f_2 + e_4 f_1^2 - 2f_2 g_5 P + d_4 P + d_8 f_0 + 2e_3 f_2 - 2f_2 h_1 - g_6 P + e_5 + g_3 = 0. \tag{39}$$

From Eq. (37), the expression of f_0 can be found as

$$f_0 = \frac{-K_1 L \pi a f_2 - d_7 f_1^2 - d_2 P - d_8 f_2 + g_8 P - d_9 - g_1}{2K_1 L \pi a + 2d_6}. \tag{40}$$

Substituting Eq. (40) into Eq. (39), the f_1 expression is achieved by

$$f_1^2 = \frac{l_3 P f_2 + l_5 f_2 + l_4 P + l_6}{l_7 f_2 + l_8}, \tag{41}$$

where

$$l_3 = -4g_5 \left(K_1 L \pi a + d_6 \right),$$

$$l_4 = -2 \left(-d_4 + g_6 \right) \left(K_1 L \pi a + d_6 \right) - K_1 L \pi a d_2 + K_1 L \pi a g_8 - d_2 d_8 + d_8 g_8,$$

$$l_5 = -2 \left(-2e_3 + 2h_1 \right) \left(K_1 L \pi a + d_6 \right) - K_1^2 L^2 \pi^2 a^2 - 2K_1 L \pi a d_8 - d_8^2,$$

$$l_6 = -2 \left(-e_5 - g_3 \right) \left(K_1 L \pi a + d_6 \right) - K_1 L \pi a d_9 - K_1 L \pi a g_1 - d_8 d_9 - d_8 g_1,$$

$$l_7 = -4e_2 \left(K_1 L \pi a + d_6 \right), l_8 = La \pi \left(d_7 - 2e_4 \right) K_1 - 2d_6 e_4 + d_7 d_8.$$

Substituting Eqs. (40) and (41) into Eq. (38), the $P - f_2$ relation is obtained by

$$P = \frac{l_9 f_2^3 + l_{10} f_2^2 + p_1 f_2 + p_2}{p_3 f_2 + p_4}, \tag{42}$$

where

$$l_9 = -2e_2l_7\left(K_1L\pi a + d_6\right), \quad l_{10} = \left(La\pi\left(d_7 - 2e_4\right)K_1 - 2d_6e_4 + d_7d_8\right)l_7 - 2l_8e_2\left(K_1L\pi a + d_6\right),$$

$$p_1 = 2\left(\left(-e_6 - g_2 + h_2\right)l_7 - e_4l_8\right)\left(K_1L\pi a + d_6\right) + K_1L\pi a\left(d_7l_8 - 4e_1l_5\right)$$
$$\quad - 4d_6e_1l_5 + d_7^2l_5 + d_7d_8l_8 + d_7d_9l_7 + d_7g_1l_7,$$

$$p_2 = 2\left(-e_6 - g_2 + h_2\right)l_8\left(K_1L\pi a + d_6\right) - 4K_1L\pi ae_1l_6 - 4d_6e_1l_6 + d_7^2l_6 + d_7d_9l_8 + d_7g_1l_8,$$

$$p_3 = 2K_1L\pi a\left(d_3l_7 + 2e_1l_3 - g_7l_7\right) - d_2d_7l_7 + 2d_3d_6l_7 + 4d_6e_1l_3 - 2d_6g_7l_7 - d_7^2l_3 + d_7g_8l_7,$$

$$p_4 = 2K_1L\pi a\left(d_3l_8 + 2e_1l_4 - g_7l_8\right) - d_2d_7l_8 + 2d_3d_6l_8 + 4d_6e_1l_4 - 2d_6g_7l_8 - d_7^2l_4 + d_7g_8l_8,$$

Applying $f_2 \to 0$, the buckling axial compressive loads P_b of FG-GPLRC cylindrical shells is achieved as

$$P_b = \frac{p_2}{p_4}. \tag{43}$$

The critical buckling axial compression load P_b^{cr} of shells is obtained to be the smallest buckling axial compressive load with the corresponding mode (m, n).

From Eq. (27), the maximal deflection is achieved by

$$W_{\max} = f_0 + f_1 + f_2. \tag{44}$$

Substituting Eqs. (40) and (41) into Eq. (44), the maximal deflection is rewritten as

$$W_{max} = \frac{1}{2K_1L\pi a + 2d_6}\left(-K_1L\pi af_2 - \frac{d_7\left(l_3Pf_2 + l_5f_2 + l_4P + l_6\right)}{l_7f_2 + l_8}\right.$$
$$\left. - d_2P - d_8f_2 + g_8P - d_9 - g_1\right) + \sqrt{\frac{l_3Pf_2 + l_5f_2 + l_4P + l_6}{l_7f_2 + l_8}} + f_2. \tag{45}$$

By varying the amplitude f_2, the axial compressive postbuckling curves are obtained by combining Eqs. (43) and (45).

4. COMPARISON RESULTS AND NUMERICAL EXAMPLES

To validate the present formulation, the dimensionless critical axial compressive loads, defined as the ratio of the critical load of the FG-GPLRC cylindrical shell to that of the corresponding polymer shell, are compared with previously published results, as presented in Table 1. The comparison demonstrates excellent agreement with different GPL distribution patterns and geometric parameters, thus confirming the accuracy and reliability of the proposed model.

Table 1. Comparison of the dimensionless critical buckling load of FG-GPLRC cylindrical shells
($h = 4$ mm, $L = 1000$ mm, $a = 200$ mm, $W_{GPL} = 0.5\%$, $K_1 = 0$ N/m^3, $K_2 = 0$ N/m)

Type	Wang, Feng, Zhao, & Yang (2018)	Ansari et al. (2020)	Present
UD	2.7409	2.7371	2.6595
FG-A	2.5099	2.5543	2.4821
FG-O	2.1792	2.2677	2.2061
FG-X	3.1961	3.1283	3.0460

In the numerical investigations, the copper/GPL FG-GPLRC is chosen, with material parameters applied as per the report by Wang et al. (2022). For simplicity, the geometrical parameters of stiffeners are chosen by satisfying $b_x = b_y = b_{hx} = b_{St}$, $d_x = d_y = d_{hx} = d_{St}$, and $h_x = h_y = h_{hx} = h_{St}$.

Table 2 evaluates the effect of orthogonal and spiral stiffeners on the critical buckling load P_b^{cr} of FG-GPLRC cylindrical shells for different GPL distribution patterns. The results indicate that both orthogonal and spiral stiffeners significantly enhance the load-carrying capacity of the shell, and the spiral stiffeners show superior performance. The superior performance of spiral stiffeners over orthogonal ones can be attributed to their ability to provide multi-directional reinforcement. Unlike orthogonal stiffeners, which primarily enhance stiffness along specific longitudinal and circumferential directions, spiral stiffeners distribute stress more uniformly across the shell. In addition, the critical buckling axial compressive load P_b^{cr} of the FG-X cylindrical shell is the highest, while that of the FG-O cylindrical shell is the smallest in all cases: unstiffened, orthogonal stiffeners, and spiral stiffeners.

Table 2. The effect of stiffener and GPL distribution patterns on P_b^{cr} (GPa) of cylindrical shell
($\Delta T = 0, h = 2$ mm, $h_{St} = b_{St} = h, L = 2\pi a n_y/n_x, n_x = 50, n_y = 12, d_{St} = L/n_y,$
$a/h = 100, W_{GPL}^* = 0.5\%, K_1 = 0$ N/m^3, $K_2 = 0$ N/m)

Type	Unstiffened	Orthogonal stiffeners	Spiral stiffeners
FG-X	1.062 (8, 4)[a]	1.187 (4, 8)	1.313 (1, 6, 40, 36.87)[b]
UD	1.015 (4, 9)	1.149 (4, 8)	1.259 (8, 1, 39, 38.74)
FG-O	0.959 (9, 1)	1.103 (4, 8)	1.209 (8, 1, 39, 38.74)
FG-V	1.000 (8, 5)	1.153 (4, 8)	1.278 (8, 1, 39, 38.74)
FG-A	1.008 (8, 5)	1.127 (4, 8)	1.221 (8, 1, 39, 38.74)

The buckling modes: [a](m, n), [b](m, n, n_{hx}, γ).

Table 3 investigates the effects of a/h ratio on the critical buckling axial compressive load P_b^{cr} of the FG-GPLRC cylindrical shells with the spiral stiffeners. As the a/h ratio increases, indicating thinner shells, the critical buckling load significantly decreases. This trend occurred in all cases and reflects the classical shell buckling characteristic, wherein slenderness increases the instability of the shell.

Table 3. The effect of stiffeners and GPL distribution patterns on P_b^{cr} (GPa) of cylindrical shell (Spiral stiffeners, $\Delta T = 0, h = 2$ mm, $h_{St} = b_{St} = h, L = 2\pi a n_y/n_x, n_x = 50, n_y = 12, d_{St} = L/n_y, W_{GPL}^* = 0.3\%,$
$K_1 = 0$ N/m^3, $K_2 = 0$ N/m)

Type	$a/h = 80$	$a/h = 100$	$a/h = 120$
FG-X	1.533 (7, 1, 39, 38.74)	1.187 (1, 6, 40, 36.87)	0.940 (1, 6, 39, 38.74)
UD	1.500 (1, 5, 40, 36.87)	1.154 (8, 1, 39, 38.74)	0.915 (1, 6, 39, 38.74)
FG-O	1.467 (1, 5, 40, 36.87)	1.124 (8, 1, 39, 38.74)	0.888 (9, 1, 38, 40.54)

Table 4 examines the effect of the number of spiral stiffeners on the critical buckling load of FG-GPLRC cylindrical shells. Importantly, while the number of spiral stiffener increases, the spacing between adjacent stiffener remains constant. As a result, the total length and volume of stiffener material are kept unchanged, ensuring that the observed changes in buckling behavior are due solely to the variation in stiffener orientation. The results indicate that increasing the number of spiral stiffeners improves the buckling resistance up to a peak at 40 stiffeners, beyond which the critical load begins to decline. The observed peak in the critical buckling load at a specific number of spiral stiffeners (or stiffener angle) is believed to result from a complex interplay between the stiffness contributions and the geometrical characteristics of the shell structure. While the present study identifies the optimal configuration under the given conditions, a more detailed investigation is required to clearly elucidate the underlying physical mechanisms.

Table 4. The effect of number of stiffeners on P_b^{cr} (GPa) of cylindrical shell (Spiral stiffeners, $\Delta T = 0$, $h = 2$ mm, $a/h = 100$, $L = 2\pi a n_y/n_x$, $n_x = 50$, $n_y = 12$, $d_{St} = L/n_y$, $W_{GPL}^* = 0.5\%$, $K_1 = 0$ N/m^3, $K_2 = 0$ N/m)

n_{hx}	FG-X	UD	FG-O
30	1.104 (8, 1, 53.13)^c	1.062 (8, 1, 53.13)	1.014 (8, 1, 53.13)
32	1.129 (8, 1, 50.21)	1.087 (8, 1, 50.21)	1.038 (8, 1, 50.21)
34	1.164 (8, 1, 47.16)	1.121 (8, 1, 47.16)	1.073 (8, 1, 47.16)
36	1.210 (8, 1, 43.95)	1.167 (8, 1, 43.95)	1.118 (8, 1, 43.95)
38	1.268 (8, 1, 40.54)	1.225 (8, 1, 40.54)	1.175 (8, 1, 40.54)
40	1.313 (1, 6, 36.87)	1.255 (1, 6, 36.87)	1.190 (1, 6, 36.87)
42	1.265 (1, 6, 32.86)	1.208 (1, 6, 32.86)	1.144 (1, 6, 32.86)
44	1.221 (1, 6, 28.36)	1.163 (1, 6, 28.36)	1.100 (1, 6, 28.36)
46	1.178 (1, 6, 23.07)	1.121 (1, 6, 23.07)	1.058 (1, 6, 23.07)
48	1.137 (1, 6, 16.26)	1.080 (1, 6, 16.26)	1.017 (1, 6, 16.26)

^{c}The buckling modes (m, n, γ).
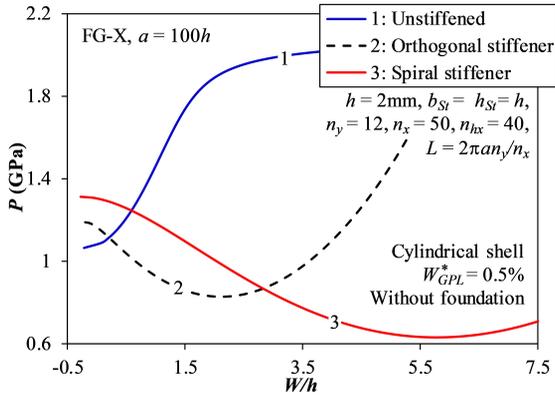
Fig. 3. Effect of stiffener type on the nonlinear post-buckling responses of FG-GPLRC cylindrical shells
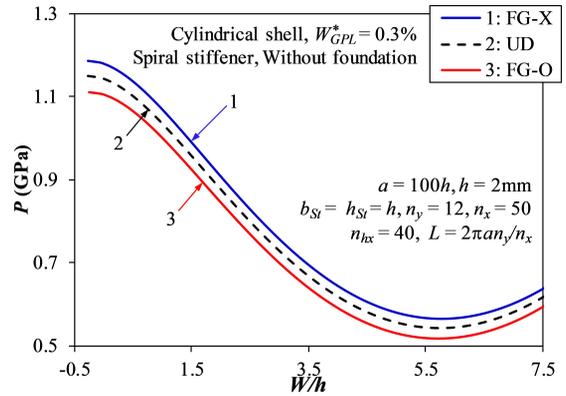

Fig. 4. Effect of GPL distribution patterns on the nonlinear postbuckling responses of FG-GPLRC cylindrical shells with spiral stiffeners

Fig. 3 investigates the effect of stiffener types (unstiffened, orthogonal stiffeners, and spiral stiffeners) on the postbuckling curves $P - W/h$ of FG-GPLRC cylindrical shells. The spiral stiffeners significantly shift the postbuckling curve upward, demonstrating enhanced structural stiffness and a substantially increased load-bearing capacity of the shells. Fig. 4 presents the effect of GPL distribution patterns on the nonlinear postbuckling behavior of spiral-stiffened cylindrical shells. FG-X cylindrical shell again shows the best axial compressive load-carrying capacity, followed by UD and FG-O. The consistent superiority of the FG-X pattern arises from its distribution of GPLs near the outer surfaces of the shell. This effectively increases the bending stiffness of the shell, enhancing its load-carrying capacity. In contrast, the FG-O pattern concentrates GPLs near the neutral axis, which contributes less to bending stiffness and therefore results in lower critical buckling loads and weaker postbuckling load-carrying capacity. These results emphasize the role of the GPL distribution pattern in optimizing structural design.

Fig. 5 explores the influence of GPL mass fraction on the nonlinear postbuckling response of FG-GPLRC cylindrical shells with spiral stiffeners. As the GPL mass fraction increases from 0.1% to 0.5%, the load-carrying capacity of the shell improves significantly. This trend reflects the advantage of the intrinsic stiffness of GPLs. When GPLs are properly distributed, the stiffness of the structure is significantly improved. As a result, the load-bearing capacity of the

shell is increased and the instability is resisted. Fig. 6 shows the postbuckling curves of the spiral-stiffened cylindrical shell with different values of the a/h ratio. As a/h increases, the postbuckling curves decrease, similar to the trend shown in Table 3. Physically, this phenomenon is due to the fact that the bending stiffness of the structures decreases as the shell thickness decreases.
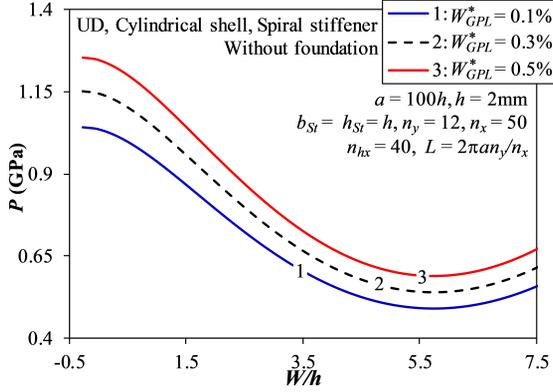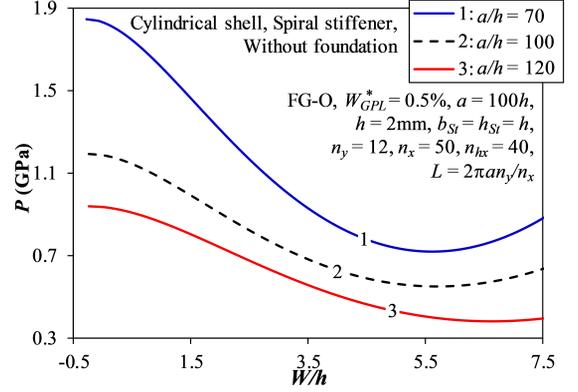

Fig. 5. Effect of GPL mass fraction on the nonlinear postbuckling responses of FG-GPLRC cylindrical shells with spiral stiffeners

Fig. 6. Effect of a/h ratio on the nonlinear post-buckling responses of cylindrical shells with spiral stiffeners
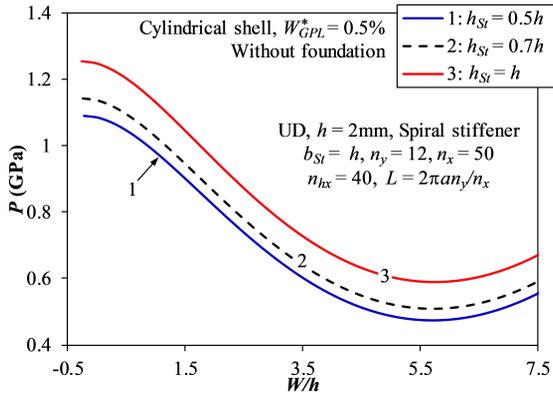

Fig. 7. Effect of spiral stiffener thickness on the nonlinear postbuckling responses of spiral-stiffened FG-GPLRC cylindrical shells
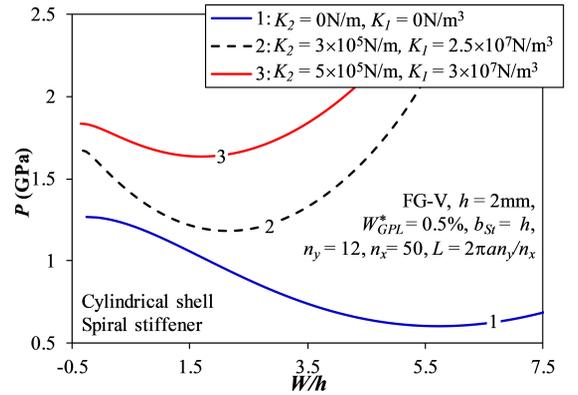

Fig. 8. Effect of elastic foundation stiffness on the critical buckling compressive load of FG-GPLRC cylindrical shells with spiral stiffeners

The effects of spiral stiffener thickness h_{St} on the nonlinear postbuckling responses of stiffened cylindrical shells are illustrated in Fig. 7. Increasing the stiffener thickness from $0.5h$ to h significantly enhances the buckling load. It is clear that increasing the height of the stiffeners also increases their volume. As a result, the overall stiffness and stability of the structure are improved. This is an important consideration when designing stiffened structures.

Fig. 8 investigates the effect of elastic foundation parameters K_1 and K_2. The results show that as the foundation stiffness increases, the load-carrying capacity of the shell increases. This benefit is especially evident when comparing the shell without a foundation to the shell resting on an elastic foundation, highlighting the supporting role of the shell-foundation interaction in enhancing mechanical stability.

5. CONCLUSIONS

This study presents a comprehensive analytical framework for analyzing the nonlinear buckling and postbuckling behavior of FG-GPLRC cylindrical shells stiffened by orthogonal or spiral FG-GPLRC stiffeners. The governing equations are established based on Donnell shell theory with geometric nonlinearity. By using the Ritz energy method, the critical buckling axial compressive loads and the load-deflection relationship are determined. The effects of spiral stiffeners, geometrical parameters, material parameters, and elastic foundation parameters are investigated in detail. Some conclusions are drawn as follows:

(1) Spiral-stiffened cylindrical shells have better load-carrying capacity than orthogonal-stiffened cylindrical shells due to the multi-directional reinforcement capability of the spiral stiffener system.

(2) FG-X stiffened cylindrical shells have the highest structural stability among all GPL patterns.

(3) Geometric, material, and elastic foundation parameters significantly influence the buckling and postbuckling behavior of spiral-stiffened FG-GPLRC cylindrical shells.

The geometric parameters of the stiffeners in this study were assumed to be equal for the sake of simplification and to align with the initial objective of evaluating the relative effectiveness of different stiffener types. Nevertheless, comprehensive future investigations involving stiffeners with varying dimensions are necessary to support practical engineering applications.

DECLARATION OF COMPETING INTEREST

The authors declare that they have no known competing financial interests or personal relationships that could have appeared to influence the work reported in this paper.

CREDIT AUTHOR STATEMENT

Kieu Quang Thai: *Investigation, Validation, Formal analysis, Writing – original draft*. Dao Huy Bich: *Conceptualization, Methodology, Supervision, Writing – review & editing*. Nguyen Thi Phuong: *Conceptualization, Methodology, Supervision, Writing – review & editing*. Cao Van Doan: *Investigation, Formal analysis, Writing – original draft*. Tran Quang Minh: *Investigation, Formal analysis, Writing – original draft*.

ACKNOWLEDGEMENT

REFERENCES

Ansari, R., & Torabi, J. (2019). Semi-analytical postbuckling analysis of polymer nanocomposite cylindrical shells reinforced with functionally graded graphene platelets. *Thin-Walled Structures*, *144*, 106248. https://doi.org/10.1016/j.tws.2019.106248

Ansari, R., Torabi, J., & Hasrati, E. (2020). Postbuckling analysis of axially-loaded functionally graded GPL-reinforced composite conical shells. *Thin-Walled Structures*, *148*, 106594. https://doi.org/10.1016/j.tws.2019.106594

Dong, D. T., Nam, V. H., Phuong, N. T., Ly, L. N., Duc, V. M., Van Tien, N., Minh, T. Q., Hung, V. T., & Quan, P. H. (2022). An analytical approach of nonlinear buckling behavior of longitudinally compressed carbon nanotube-reinforced (CNTR) cylindrical shells with CNTR stiffeners in thermal environment. *ZAMM - Journal of Applied Mathematics and Mechanics / Zeitschrift für Angewandte Mathematik und Mechanik*, *102*(4), e202100228. https://doi.org/10.1002/zamm.202100228

Huang, H., & Han, Q. (2009). Nonlinear elastic buckling and postbuckling of axially compressed functionally graded cylindrical shells. *International Journal of Mechanical Sciences*, *51*(7), 500–507. https://doi.org/10.1016/j.ijmecsci.2009.05.002

Huang, X., Yang, J., & Yang, Z. (2021). Thermo-elastic analysis of functionally graded graphene nanoplatelets (GPLs) reinforced closed cylindrical shells. *Applied Mathematical Modelling*, *97*, 754–770. https://doi.org/10.1016/j.apm.2021.04.027

Huy Bich, D., Van Dung, D., Nam, V. H., & Thi Phuong, N. (2013). Nonlinear static and dynamic buckling analysis of imperfect eccentrically stiffened functionally graded circular cylindrical thin shells under axial compression. *International Journal of Mechanical Sciences*, *74*, 190–200. https://doi.org/10.1016/j.ijmecsci.2013.06.002

Jiao, P., Chen, Z., Li, Y., Ma, H., & Wu, J. (2019). Dynamic buckling analyses of functionally graded carbon nanotubes reinforced composite (FG-CNTRC) cylindrical shell under axial power-law time-varying displacement load. *Composite Structures*, *220*, 784–797. https://doi.org/10.1016/j.compstruct.2019.04.048

Lei, Z., Liew, K., & Yu, J. (2013). Large deflection analysis of functionally graded carbon nanotube-reinforced composite plates by the element-free kp-Ritz method. *Computer Methods in Applied Mechanics and Engineering*, *256*, 189–199. https://doi.org/10.1016/j.cma.2012.12.007

Liu, D., Kitipornchai, S., Chen, W., & Yang, J. (2018). Three-dimensional buckling and free vibration analyses of initially stressed functionally graded graphene reinforced composite cylindrical shell. *Composite Structures*, *189*, 560–569. https://doi.org/10.1016/j.compstruct.2018.01.106

Lu, L., Leanza, S., Liu, Y., & Zhao, R. R. (2025). Buckling and post-buckling of cylindrical shells under combined torsional and axial loads. *European Journal of Mechanics - A/Solids*, *112*, 105653. https://doi.org/10.1016/j.euromechsol.2025.105653

Nam, V. H., Phuong, N. T., Van Minh, K., & Hieu, P. T. (2018). Nonlinear thermo-mechanical buckling and post-buckling of multilayer FGM cylindrical shell reinforced by spiral stiffeners surrounded by elastic foundation subjected to torsional loads. *European Journal of Mechanics - A/Solids*, *72*, 393–406. https://doi.org/10.1016/j.euromechsol.2018.06.005

Nguyen, T. N., Lee, S., Nguyen, P.-C., Nguyen-Xuan, H., & Lee, J. (2020). Geometrically nonlinear postbuckling behavior of imperfect FG-CNTRC shells under axial compression using isogeometric analysis. *European Journal of Mechanics - A/Solids*, *84*, 104066. https://doi.org/10.1016/j.euromechsol.2020.104066

Ramezani, M., Rezaiee-Pajand, M., & Tornabene, F. (2022). Nonlinear thermomechanical analysis of GPLRC cylindrical shells using HSDT enriched by quasi-3D ANS cover functions. *Thin-Walled Structures*, *179*, 109582. https://doi.org/10.1016/j.tws.2022.109582

Shen, H.-S. (2005). Postbuckling of axially loaded FGM hybrid cylindrical shells in thermal environments. *Composites Science and Technology*, *65*(11–12), 1675–1690. https://doi.org/10.1016/j.compscitech.2005.02.008

Shen, H.-S. (2011). Postbuckling of nanotube-reinforced composite cylindrical shells in thermal environments, Part I: Axially-loaded shells. *Composite Structures*, *93*(8), 2096–2108. https://doi.org/10.1016/j.compstruct.2011.02.011

Shen, H.-S., & Xiang, Y. (2013). Postbuckling of nanotube-reinforced composite cylindrical shells under combined axial and radial mechanical loads in thermal environment. *Composites Part B: Engineering*, *52*, 311–322. https://doi.org/10.1016/j.compositesb.2013.04.034

Singh, R., Gupta, A., & Jain, N. K. (2025). Free vibration analysis of cracked isotropic and FGM cylindrical shells with axially varying thickness: An analytical approach. *Thin-Walled Structures*, *2025*, 113344. https://doi.org/10.1016/j.tws.2025.113344

Sofiyev, A. H., & Kuruoglu, N. (2014). Buckling and vibration of shear deformable functionally graded orthotropic cylindrical shells under external pressures. *Thin-Walled Structures*, *78*, 121–130. https://doi.org/10.1016/j.tws.2014.01.009

Wang, Y., Zeng, R., & Safarpour, M. (2022). Vibration analysis of FG-GPLRC annular plate in a thermal environment. *Mechanics Based Design of Structures and Machines*, *50*(1), 352–370. https://doi.org/10.1080/15397734.2020.1719508

Wang, Y., Feng, C., Zhao, Z., Lu, F., & Yang, J. (2018). Torsional buckling of graphene platelets (GPLs) reinforced functionally graded cylindrical shell with cutout. *Composite Structures*, *197*, 72–79. https://doi.org/10.1016/j.compstruct.2018.05.056

Wang, Y., Feng, C., Zhao, Z., & Yang, J. (2018). Eigenvalue buckling of functionally graded cylindrical shells reinforced with graphene platelets (GPL). *Composite Structures*, *202*, 38–46. https://doi.org/10.1016/j.compstruct.2017.10.005